Collaborative Autonomous Vehicles with Signals of Opportunity Aided Inertial Navigation Systems

Joshua J. Morales, Joe Khalife, and Zaher M. Kassas
University of California, Riverside

BIOGRAPHIES

Joshua J. Morales is pursuing a Ph.D. from the Department of Electrical and Computer Engineering at the University of California, Riverside and is a member of the Autonomous Systems Perception, Intelligence, and Navigation (ASPIN) Laboratory. He received a B.S. in Electrical Engineering with High Honors from the University of California, Riverside. His research interests include estimation, navigation, autonomous vehicles, and intelligent transportation systems.

Joe Khalife is pursuing a Ph.D. from the Department of Electrical and Computer Engineering at the University of California, Riverside and is a member of the ASPIN Laboratory. He received a B.E. in Electrical Engineering and an M.S. in Computer Engineering from the Lebanese American University (LAU). From 2012 to 2015, he was a research assistant at LAU. His research interests include opportunistic navigation, autonomous vehicles, and software-defined radio.

Zaher (Zak) M. Kassas is an assistant professor at the University of California, Riverside and director of the ASPIN Laboratory. He received a B.E. in Electrical Engineering from the Lebanese American University, an M.S. in Electrical and Computer Engineering from The Ohio State University, and an M.S.E. in Aerospace Engineering and a Ph.D. in Electrical and Computer Engineering from The University of Texas at Austin. From 2004 through 2010 he was a research and development engineer with the LabVIEW Control Design and Dynamical Systems Simulation Group at National Instruments Corp. His research interests include estimation, navigation, autonomous vehicles, and intelligent transportation systems.

ABSTRACT

A collaborative signal of opportunity (SOP)-aided inertial navigation system (INS) framework is presented and studied. The following problem is considered. Multiple autonomous vehicles (AVs) with access to global navigation satellite system (GNSS) signals are aiding their on-board INSs with GNSS pseudoranges. While navigating, AV-mounted receivers draw pseudorange observations on ambient unknown terrestrial SOPs and collaboratively estimate the SOPs' states. After some time, GNSS signals become unavailable. Subsequently, the AVs exploit the SOPs to collaboratively aid their INSs. A collaborative estimation framework which uses time-difference-of-arrival (TDOA) measurements taken with reference to a specific SOP is presented. This framework is studied over varying the quantity of collaborating AVs, and it is demonstrated that "GNSS-like" performance can be achieved in the absence of GNSS signals. Experimental results are presented demonstrating multiple unmanned aerial vehicles (UAVs) collaboratively navigating exclusively with their onboard inertial measurement units (IMUs) and pseudoranges extracted from unknown terrestrial SOPs emanating from two cellular towers.

I. INTRODUCTION

Autonomous vehicles (AVs) will require more accurate and reliable navigation systems than ever before to operate safely and efficiently. Traditional navigation systems integrate global navigation satellite system (GNSS) with an inertial navigation system (INS). It is well known that if GNSS signals become unavailable, the errors of the INS's navigation solution diverge. Recently, signals of opportunity (SOPs) have been considered to enable navigation whenever GNSS signals become inaccessible or untrustworthy [1–5]. Not only could SOPs provide a navigation solution in a standalone fashion [6–8], but also SOPs could be used as an aiding source for an INS to establish a

Preprint of the 2017 ION ITM Conference
Monterey, CA, January 30–February 2, 2017

bound on INS errors in the absence of GNSS signals [9]. Collaborating AVs could share information gathered from SOPs to further reduce the bounds on INS errors [4].

Fusing GNSS and inertial measurement unit (IMU) measurements with loosely-coupled, tightly-coupled, and deeply-coupled integration strategies are well-studied [10]. Regardless of the coupling type, the errors of a GNSS-aided INS will diverge in the absence of GNSS signals, and the divergence rate becomes dependent on the quality of the IMU. Consumer and small-scale applications that use affordable micro-electro-mechanical systems (MEMS)-grade IMUs are particularly susceptible to large error divergence rates. While high quality IMUs may reduce the rate of error divergence, they may violate cost, size, weight, and/or power constraints.

Current trends to supplement an AV's navigation system in the event that GNSS signals become unusable are traditionally sensor-based (e.g., cameras [11], lasers [12], and sonar [13]). However, SOPs (e.g., AM/FM radio [14,15], cellular [6,7,16,17], digital television [18,19], iridium [20,21], and Wi-Fi [22,23]) are free to use and could alleviate the need for costly aiding-sensors. In [24], a board-mounted transceiver equipped with an IMU was presented along with experimental results demonstrating the use of SOP Doppler measurements to aid an INS. In [9], a preliminary study of a novel tightly-coupled SOP-aided INS framework that fused IMU data with SOP pseudoranges along with GNSS pseudoranges (when available) was conducted. It was demonstrated that bounds could be established on the estimation errors in the absence of GNSS. The sensitivity of these bounds was studied for a varying quantity and quality of exploited SOPs. In this paper the SOP-aided INS framework discussed in [9] is extended to include collaborating AVs.

SOPs are abundant in GNSS-challenged environments, making them particularly attractive aiding sources for an INS whenever GNSS signals become unavailable. However, unlike GNSS where the states of satellite vehicles (SVs) are readily available, the states of SOPs (positions, clock biases, and clock drifts) may not be known *a priori* and must be estimated. This estimation problem is analogous to the simultaneous localization and mapping (SLAM) problem in robotics [25]. Both problems ask if it is possible for an AV to start at an unknown location in an unknown environment and then incrementally build a map of the environment while simultaneously localizing itself within this map. However, in contrast to the static environmental map of the typical SLAM problem, the SOP map is more complex– it is dynamic and stochastic. Specifically, for pseudorange-only observations, one must estimate not only the position and velocity states, but also the clock states of both the AV-mounted receiver and the SOPs.

In collaborative SLAM (C-SLAM), multiple AVs share their pose estimates and observations in order to improve the quality of their individual state estimates and to build a larger and more accurate map [26]. In this work, multiple collaborating AVs will be estimating their states (attitude, position, velocity, clock bias, and clock drift) in a three-dimensional (3-D) environment and will make mutual observations on the dynamic and stochastic SOP map. Specifically, SOP pseudorange observations will be shared and the time-of-arrival (TOA) and time-difference-of-arrival (TDOA) will be considered.

This paper considers an environment comprising multiple AVs and multiple unknown SOPs. Each AV is assumed to have access to GNSS SV pseudoranges, multiple unknown terrestrial SOP pseudoranges, and an onboard IMU. While GNSS pseudoranges are available, the AVs collaboratively map the SOPs, estimating the SOPs' positions, clock biases, and clock drifts. During this mode, the UAVs are navigating with a tightly-coupled GNSS-aided INS strategy. Suddenly, GNSS pseudoranges become unavailable. The AVs continue drawing pseudorange observables from the SOPs and continue estimating the SOPs' states. In this mode, the AVs switch to navigating with a collaborative tightly-coupled SOP-aided INS strategy. This paper will formulate this proposed strategy and study how the uncertainty bounds are affected by varying the quantity of collaborating AVs. It is demonstrated that AVs equipped with consumer-grade IMUs navigating with the proposed strategy could achieve a performance comparable to when GNSS signals are still available.

The remainder of this paper is organized as follows. Section II describes the dynamics model of the SOPs and navigating vehicles as well as the receivers' observation model. Section III describes the collaborative SOP-aided INS framework. Section IV presents simulation results demonstrating the performance of the framework and compares the performance for a varying number of collaborating AVs. Section V presents experimental results of collaborating AVs using cellular signals to aid their INSs. Concluding remarks are given in Section VI.

II. MODEL DESCRIPTION

A. SOP Dynamics Model

Each SOP will be assumed to emanate from a spatially-stationary terrestrial transmitter, and its state vector will consist of its 3-D position states $\boldsymbol{r}_{\text{sop}_m} \triangleq \left[x_{\text{sop}_m},\, y_{\text{sop}_m},\, z_{\text{sop}_m}\right]^{\mathsf{T}}$ and clock error states $\boldsymbol{x}_{\text{clk,sop}_m} \triangleq \left[c\delta t_{\text{sop}_m},\, c\dot{\delta} t_{\text{sop}_m}\right]^{\mathsf{T}}$, where c is the speed of light, δt_{sop_m} is the clock bias, $\dot{\delta} t_{\text{sop}_m}$ is the clock drift, $m = 1, \ldots, M$, and M is the total number of SOPs.

The SOP's discretized dynamics are given by

$$\boldsymbol{x}_{\text{sop}_m}(k+1) = \mathbf{F}_{\text{sop}}\, \boldsymbol{x}_{\text{sop}_m}(k) + \boldsymbol{w}_{\text{sop}_m}(k), \quad k = 1, 2, \ldots, \tag{1}$$

where $\boldsymbol{x}_{\text{sop}_m} = \left[\boldsymbol{r}_{\text{sop}_m}^{\mathsf{T}},\, \boldsymbol{x}_{\text{clk,sop}_m}^{\mathsf{T}}\right]^{\mathsf{T}}$, $\mathbf{F}_{\text{sop}} = \text{diag}\left[\mathbf{I}_{3\times 3},\, \mathbf{F}_{\text{clk}}\right]$, $\boldsymbol{w}_{\text{sop}_m}$ is the process noise, which is modeled as a discrete-time (DT) zero-mean white noise sequence with covariance $\mathbf{Q}_{\text{sop}_m} = \text{diag}\left[\mathbf{0}_{3\times 3},\, c^2\mathbf{Q}_{\text{clk,sop}_m}\right]$, and

$$\mathbf{F}_{\text{clk}} = \begin{bmatrix} 1 & T \\ 0 & 1 \end{bmatrix}, \quad \mathbf{Q}_{\text{clk,sop}_m} = \begin{bmatrix} S_{w_{\delta t_{\text{sop}_m}}} T + S_{w_{\dot{\delta} t_{\text{sop}_m}}} \frac{T^3}{3} & S_{w_{\dot{\delta} t_{\text{sop}_m}}} \frac{T^2}{2} \\ S_{w_{\dot{\delta} t_{\text{sop}_m}}} \frac{T^2}{2} & S_{w_{\dot{\delta} t_{\text{sop}_m}}} T \end{bmatrix},$$

where T is the constant sampling interval. The terms $S_{w_{\delta t_{\text{sop}_m}}}$ and $S_{w_{\dot{\delta} t_{\text{sop}_m}}}$ are the clock bias and drift process noise power spectra, respectively, which can be related to the power-law coefficients, $\left\{h_{\alpha,\text{sop}_m}\right\}_{\alpha=-2}^{2}$, which have been shown through laboratory experiments to characterize the power spectral density of the fractional frequency deviation of an oscillator from nominal frequency according to $S_{w_{\delta t_{\text{sop}_m}}} \approx \frac{h_{0,\text{sop}_m}}{2}$ and $S_{w_{\dot{\delta} t_{\text{sop}_m}}} \approx 2\pi^2 h_{-2,\text{sop}_m}$ [27].

B. Vehicle Dynamics Model

The n^{th} AV-mounted navigating receiver's state vector $\boldsymbol{x}_{r_n}$ is comprised of the INS states $\boldsymbol{x}_{B_n}$ and the receiver's clock states $\boldsymbol{x}_{\text{clk},r_n} \triangleq \left[c\delta t_{r_n},\, c\dot{\delta} t_{r_n}\right]^{\mathsf{T}}$, i.e., $\boldsymbol{x}_{r_n} = \left[\boldsymbol{x}_{B_n}^{\mathsf{T}},\, \boldsymbol{x}_{\text{clk},r_n}^{\mathsf{T}}\right]^{\mathsf{T}}$ where $n = 1, \ldots, N$, and N is the total number of AVs.

The INS 16-state vector is

$$\boldsymbol{x}_{B_n} = \left[{}_{G}^{B}\bar{\boldsymbol{q}}_n^{\mathsf{T}},\quad \boldsymbol{r}_{r_n}^{\mathsf{T}},\quad \boldsymbol{v}_{r_n}^{\mathsf{T}},\quad \boldsymbol{b}_{g_n}^{\mathsf{T}},\quad \boldsymbol{b}_{a_n}^{\mathsf{T}}\right]^{\mathsf{T}},$$

where ${}_{G}^{B}\bar{\boldsymbol{q}}_n$ is the 4-D unit quaternion in vector-scalar form which represents the orientation of the body frame with respect to a global frame [28], e.g., the Earth-centered inertial (ECI) frame; $\boldsymbol{r}_{r_n}$ and $\boldsymbol{v}_{r_n}$ are the 3-D position and velocity, respectively, of the AV's body frame expressed in a global frame; and $\boldsymbol{b}_{g_n}$ and $\boldsymbol{b}_{a_n}$ are the gyroscope and accelerometer biases, respectively.

B.1 Receiver Clock State Dynamics

The n^{th} AV-mounted receiver's clock states will evolve in time according to

$$\boldsymbol{x}_{\text{clk},r_n}(k+1) = \mathbf{F}_{\text{clk}}\boldsymbol{x}_{\text{clk},r_n}(k) + \boldsymbol{w}_{\text{clk},r_n}(k), \tag{2}$$

where $\boldsymbol{w}_{\text{clk},r_n}$ is the process noise vector, which is modeled as a DT zero-mean white noise sequence with covariance $\mathbf{Q}_{\text{clk},r_n}$, which has an identical form to $\mathbf{Q}_{\text{clk,sop}_m}$, except that $S_{w_{\delta t_{\text{sop}_m}}}$ and $S_{w_{\dot{\delta} t_{\text{sop}_m}}}$ are now replaced with receiver-specific spectra $S_{w_{\delta t_{r_n}}}$ and $S_{w_{\dot{\delta} t_{r_n}}}$, respectively.

B.2 INS State Dynamics

The IMU on the n^{th} AV contains a triad-gyroscope and a triad-accelerometer which produce measurements $\boldsymbol{z}_{\text{imu}_n} \triangleq \left[\boldsymbol{\omega}_{\text{imu}_n}^{\mathsf{T}},\, \boldsymbol{a}_{\text{imu}_n}^{\mathsf{T}}\right]^{\mathsf{T}}$ of the angular rate and specific force, which are modeled as

$$\boldsymbol{\omega}_{\text{imu}_n} = {}^{B}\boldsymbol{\omega}_n + \boldsymbol{b}_{g_n} + \boldsymbol{n}_{g_n}$$

$$\boldsymbol{a}_{\text{imu}_n} = \mathbf{R}\left[{}^{B_k}_{G}\bar{\boldsymbol{q}}_n\right]\left({}^{G}\boldsymbol{a}_n - {}^{G}\boldsymbol{g}_n\right) + \boldsymbol{b}_{a_n} + \boldsymbol{n}_{a_n},$$

where ${}^{B}\boldsymbol{\omega}_n$ is the 3-D rotational rate vector, ${}^{G}\boldsymbol{a}_n$ is the 3-D acceleration of the IMU in the global frame, ${}^{B_k}_{G}\bar{\boldsymbol{q}}_n$ represents the orientation of the body frame in a global frame at time-step k, $\mathbf{R}\left[\bar{\boldsymbol{q}}_n\right]$ is the equivalent rotation matrix of $\bar{\boldsymbol{q}}_n$, ${}^{G}\boldsymbol{g}_n$ is the acceleration due to gravity of the n^{th} AV in the global frame, and $\boldsymbol{n}_{g_n}$ and $\boldsymbol{n}_{a_n}$ are measurement noise vectors, which are modeled as zero-mean white noise sequences with covariances $\sigma^2_{g_n}\mathbf{I}_{3\times 3}$ and $\sigma^2_{a_n}\mathbf{I}_{3\times 3}$, respectively. It is worth noting that a non-rotating global reference frame is assumed in the above IMU measurement models. For rotating frames, such as the Earth-centered Earth-fixed frame (ECEF), the rotation rate of the Earth and the Coriolis force should also be modeled, as discussed in [29].

The orientation of the INS will evolve in DT according to

$${}^{B_{k+1}}_{G}\bar{\boldsymbol{q}}_n = {}^{B_{k+1}}_{B_k}\bar{\boldsymbol{q}}_n \otimes {}^{B_k}_{G}\bar{\boldsymbol{q}}_n, \tag{3}$$

where ${}^{B_{k+1}}_{B_k}\bar{\boldsymbol{q}}_n$ represents the relative rotation of the n^{th} AV's body frame from time-step k to $k+1$ and $\otimes$ is the quaternion multiplication operator. The unit quaternion ${}^{B_{k+1}}_{B_k}\bar{\boldsymbol{q}}_n$ is the solution to the differential equation

$${}^{B_t}_{B_k}\dot{\bar{\boldsymbol{q}}}_n = \frac{1}{2}\boldsymbol{\Omega}\left[{}^{B}\boldsymbol{\omega}_n(t)\right]{}^{B_t}_{B_k}\bar{\boldsymbol{q}}_n, \quad t \in [t_k, t_{k+1}], \tag{4}$$

where $t_k \triangleq kT$ and for any vector $\boldsymbol{\omega} \in \mathbb{R}^3$, the matrix $\boldsymbol{\Omega}\left[\boldsymbol{\omega}\right]$ is defined as

$$\boldsymbol{\Omega}\left[\boldsymbol{\omega}\right] \triangleq \begin{bmatrix} -\lfloor\boldsymbol{\omega}\times\rfloor & \boldsymbol{\omega} \\ -\boldsymbol{\omega}^{\mathsf{T}} & 0 \end{bmatrix}, \quad \lfloor\boldsymbol{\omega}\times\rfloor \triangleq \begin{bmatrix} 0 & \omega_3 & -\omega_2 \\ -\omega_3 & 0 & \omega_1 \\ \omega_2 & -\omega_1 & 0 \end{bmatrix}$$

where ω_i are the elements of the vector $\boldsymbol{\omega}$.

The velocity will evolve in time according to

$$\boldsymbol{v}_{r_n}(k+1) = \boldsymbol{v}_{r_n}(k) + \int_{t_k}^{t_{k+1}} {}^{G}\boldsymbol{a}_n(\tau)d\tau. \tag{5}$$

The position will evolve in time according to

$$\boldsymbol{r}_{r_n}(k+1) = \boldsymbol{r}_{r_n}(k) + \int_{t_k}^{t_{k+1}} \boldsymbol{v}_{r_n}(\tau)d\tau. \tag{6}$$

The evolution of $\boldsymbol{b}_{g_n}$ and $\boldsymbol{b}_{a_n}$ will be modeled as random walk processes, i.e., $\dot{\boldsymbol{b}}_{a_n} = \boldsymbol{w}_{a_n}$ and $\dot{\boldsymbol{b}}_{g_n} = \boldsymbol{w}_{g_n}$ with $\mathbb{E}[\boldsymbol{w}_{g_n}] = \mathbb{E}[\boldsymbol{w}_{a_n}] = \mathbf{0}$, $\text{cov}[\boldsymbol{w}_{g_n}] = \sigma^2_{w_{g_n}}\mathbf{I}_3$, and $\text{cov}[\boldsymbol{w}_{a_n}] = \sigma^2_{w_{a_n}}\mathbf{I}_3$. The above attitude, position, and velocity models are discussed in detail in [30].

C. Receiver Observation Model

The pseudorange observation made by the n^{th} receiver on the m^{th} SOP, after discretization and mild approximations discussed in [31], is related to the receiver's and SOP's states by

$$z_{r_n,\text{sop}_m}(j) = \|\boldsymbol{r}_{r_n}(j) - \boldsymbol{r}_{\text{sop}_m}\|_2 + c\cdot\left[\delta t_{r_n}(j) - \delta t_{\text{sop}_m}(j)\right] + v_{r_n,\text{sop}_m}(j), \tag{7}$$

where v_{r_n,sop_m} is modeled as a DT zero-mean white Gaussian sequence with variance $\sigma^2_{r_n,\text{sop}_m}$. The pseudorange observation made by the n^{th} receiver on the l^{th} GNSS SV, after compensating for ionospheric and tropospheric delays is related to the receiver states by

$$z_{r_n,\text{sv}_l}(j) = \|\boldsymbol{r}_{r_n}(j) - \boldsymbol{r}_{\text{sv}_l}(j)\|_2 + c\cdot[\delta t_{r_n}(j) - \delta t_{\text{sv}_l}(j)] + v_{r_n,\text{sv}_l}(j), \tag{8}$$

where, $z_{r_n,\text{sv}_l} \triangleq z'_{r_n,\text{sv}_l} - c\delta t_{\text{iono}} - c\delta t_{\text{tropo}}$, δt_{iono} and δt_{tropo} are the ionospheric and tropospheric delays, respectively, z'_{r_n,sv_l} is the uncorrected pseudorange, v_{r_n,sv_l} is modeled as a DT zero-mean white Gaussian sequence with variance $\sigma^2_{r_n,\text{sv}_l}$, $l = 1,\ldots,L$, and L is the total number of GNSS SVs.

III. COLLABORATIVE SOP-AIDED INERTIAL NAVIGATION

In this section, the collaborative SOP-aided INS framework is described in detail.

A. Problem Formulation

Consider N navigating AVs, each of which is equipped with an IMU and receivers capable of producing pseudoranges to the same L GNSS SVs and M unknown SOPs. The goal of the collaborative SOP-aided INS framework is threefold. First, when GNSS pseudoranges are available, SOP pseudoranges will be used to (1) map all available SOPs in the AVs' vicinity and (2) supplement a GNSS-aided INS to improve the accuracy of the navigation solution. Second, when GNSS pseudoranges become unavailable, the pseudoranges drawn from the mapped SOPs will be used exclusively as an aiding source to correct the accumulating errors of their INSs. Third, the IMU data, GNSS and SOP pseudoranges, and state estimates of all collaborating AVs are shared through an extended Kalman filter (EKF)-based central fusion center (CFC) to improve the estimation performance compared to a single AV using an SOP-aided INS as was described in [9].

To exploit SOPs for navigation, their states must be known [32, 33]. However, in many practical scenarios, the SOP transmitter positions are unknown. Furthermore, the SOPs' clock states are dynamic and stochastic; therefore, they must be continuously estimated. To tackle these problems, a C-SLAM-type framework is adapted that operates in a collaborative mapping mode when GNSS psuedoranges are available and in a C-SLAM mode when GNSS pseudoranges are unavailable. A high-level diagram of this framework is illustrated in Fig. 1. In the following subsections, each mode of the collaborative SOP-aided INS framework is described.

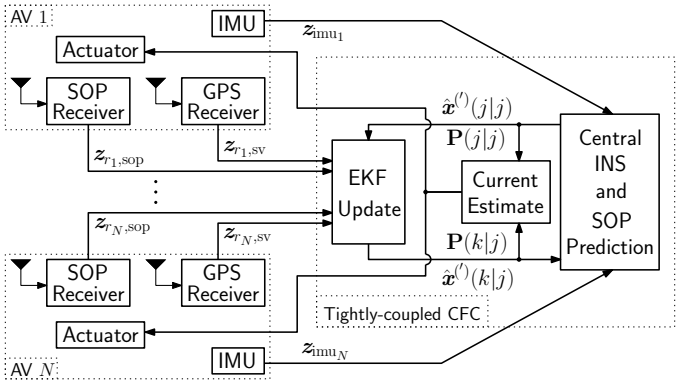

Fig. 1. Centralized collaborative SOP-aided INS that produces a state estimate $\hat{\boldsymbol{x}}^{(\prime)}$ and an estimation error covariance $\mathbf{P}$. All N collaborating AVs send their IMU data $\boldsymbol{z}_{\text{imu}_n}$, GNSS pseudoranges $\boldsymbol{z}_{r_n,\text{sv}}$, and SOP pseudoranges $\boldsymbol{z}_{r_n,\text{sop}}$ to a tightly-coupled EKF-based CFC which operates in two modes: (1) collaborative mapping mode: $\hat{\boldsymbol{x}}^{(\prime)} \equiv \hat{\boldsymbol{x}}$ and $\mathbf{P} \equiv \mathbf{P}_{\boldsymbol{x}}$, where $\hat{\boldsymbol{x}}$ and $\mathbf{P}_{\boldsymbol{x}}$ are the state estimate and the estimation error covariance, respectively, or (2) C-SLAM mode: $\hat{\boldsymbol{x}}^{(\prime)} \equiv \hat{\boldsymbol{x}}'$ and $\mathbf{P} \equiv \mathbf{P}_{\boldsymbol{x}'}$, where $\hat{\boldsymbol{x}}'$ and $\mathbf{P}_{\boldsymbol{x}'}$ are the state estimate and the estimation error covariance, respectively.

B. Collaborative Mapping Mode

In this subsection, the collaborative mapping mode is described. During this mode, all AV-mounted receivers have access to GNSS and SOP signals.

B.1 Error State Model

During the collaborative mapping mode, the EKF produces an estimate $\hat{\boldsymbol{x}}(k|j) \triangleq \mathbb{E}[\boldsymbol{x}(k)|\{\boldsymbol{z}(i)\}_{i=1}^{j}]$ of $\boldsymbol{x}(k)$ and an associated estimation error covariance $\mathbf{P}_{\boldsymbol{x}}(k|j) \triangleq \mathbb{E}[\tilde{\boldsymbol{x}}(k|j)\tilde{\boldsymbol{x}}^{\mathsf{T}}(k|j)]$. In what follows, it is assumed that $k \geq j$ and j is the last time-step an INS-aiding source was available, and

$$\boldsymbol{x} \triangleq \left[\boldsymbol{x}_{r_1}^{\mathsf{T}}, \ldots, \boldsymbol{x}_{r_N}^{\mathsf{T}}, \boldsymbol{x}_{\text{sop}_1}^{\mathsf{T}}, \ldots, \boldsymbol{x}_{\text{sop}_M}^{\mathsf{T}}\right]^{\mathsf{T}}, \ \boldsymbol{z} \triangleq \left[\boldsymbol{z}_{\text{sv}}^{\mathsf{T}}, \boldsymbol{z}_{\text{sop}}^{\mathsf{T}}\right]^{\mathsf{T}},$$

$$\boldsymbol{z}_{\text{sv}} \triangleq \left[\boldsymbol{z}_{r_1,\text{sv}}^{\mathsf{T}}, \ldots, \boldsymbol{z}_{r_N,\text{sv}}^{\mathsf{T}}\right]^{\mathsf{T}}, \quad \boldsymbol{z}_{\text{sop}} \triangleq \left[\boldsymbol{z}_{r_1,\text{sop}}^{\mathsf{T}}, \ldots, \boldsymbol{z}_{r_N,\text{sop}}^{\mathsf{T}}\right]^{\mathsf{T}},$$

$$\boldsymbol{z}_{r_n,\mathrm{sv}} = \left[z_{r_n,\mathrm{sv}_1}, \ldots, z_{r_n,\mathrm{sv}_L}\right]^{\mathsf{T}}, \quad \boldsymbol{z}_{r_n,\mathrm{sop}} = \left[z_{r_n,\mathrm{sop}_1}, \ldots, z_{r_n,\mathrm{sop}_M}\right]^{\mathsf{T}}.$$

The EKF error state is defined as

$$\tilde{\boldsymbol{x}} \triangleq \left[\tilde{\boldsymbol{x}}_{B_1}^{\mathsf{T}}, \tilde{\boldsymbol{x}}_{\mathrm{clk},r_1}^{\mathsf{T}}, \ldots, \tilde{\boldsymbol{x}}_{B_N}^{\mathsf{T}}, \tilde{\boldsymbol{x}}_{\mathrm{clk},r_N}^{\mathsf{T}} \tilde{\boldsymbol{r}}_{\mathrm{sop}_1}^{\mathsf{T}}, \tilde{\boldsymbol{x}}_{\mathrm{clk},\mathrm{sop}_1}^{\mathsf{T}}, \ldots, \tilde{\boldsymbol{r}}_{\mathrm{sop}_M}^{\mathsf{T}}, \tilde{\boldsymbol{x}}_{\mathrm{clk},\mathrm{sop}_M}^{\mathsf{T}}\right]^{\mathsf{T}}, \tag{9}$$

where

$$\tilde{\boldsymbol{x}}_{B_n} = \begin{bmatrix}\tilde{\boldsymbol{\theta}}_n^{\mathsf{T}} & \tilde{\boldsymbol{r}}_{r_n}^{\mathsf{T}} & \tilde{\boldsymbol{v}}_{r_n}^{\mathsf{T}} & \tilde{\boldsymbol{b}}_{g_n}^{\mathsf{T}} & \tilde{\boldsymbol{b}}_{a_n}^{\mathsf{T}}\end{bmatrix}^{\mathsf{T}},$$

where $\tilde{\boldsymbol{\theta}}_n \in \mathbb{R}^3$ is the 3-axis error angle vector. The position, velocity, and clock errors are defined as the standard additive error, e.g., $\tilde{\boldsymbol{r}}_{\mathrm{sop}_1} \triangleq \boldsymbol{r}_{\mathrm{sop}_1} - \hat{\boldsymbol{r}}_{\mathrm{sop}_1}$. The orientation error is related through the quaternion product

$${}^{B}_{G}\bar{\boldsymbol{q}}_n = {}^{B}_{G}\hat{\bar{\boldsymbol{q}}}_n \otimes \delta\bar{\boldsymbol{q}}_n,$$

where the error quaternion $\delta\bar{\boldsymbol{q}}_n$ is the small deviation of the estimate ${}^{B}_{G}\hat{\bar{\boldsymbol{q}}}_n$ from the true orientation ${}^{B}_{G}\bar{\boldsymbol{q}}_n$ and is given by

$$\delta\bar{\boldsymbol{q}}_n = \begin{bmatrix}\frac{1}{2}\tilde{\boldsymbol{\theta}}_n^{\mathsf{T}}, \sqrt{1 - \frac{1}{4}\tilde{\boldsymbol{\theta}}_n^{\mathsf{T}}\tilde{\boldsymbol{\theta}}_n}\end{bmatrix}^{\mathsf{T}}.$$

B.2 State Propagation

Between aiding updates, the central INS uses $\{\boldsymbol{z}_{\mathrm{imu}_n}\}_{n=1}^{N}$ and the dynamics discussed in Section II to propagate the estimate and produce the corresponding prediction error covariance. The SOP state estimate propagation follows from (1) and is given by

$$\hat{\boldsymbol{x}}_{\mathrm{sop}_m}(k+1|j) = \mathbf{F}_{\mathrm{sop}}\,\hat{\boldsymbol{x}}_{\mathrm{sop}_m}(k|j).$$

Since the gyroscope and accelerometer biases evolve according to a random walk, their state estimate propagation equations are given by

$$\hat{\boldsymbol{b}}_{g_n}(k+1|j) = \hat{\boldsymbol{b}}_{g_n}(k|j) \quad \text{and} \quad \hat{\boldsymbol{b}}_{a_n}(k+1|j) = \hat{\boldsymbol{b}}_{a_n}(k|j).$$

In order to propagate the receiver's orientation state estimate, the differential equation in (4) must be solved. In this paper, a fourth order Runge-Kutta method is employed and the solution to (4) is given by

$${}^{B_{k+1}}_{B_k}\hat{\bar{\boldsymbol{q}}}_n = \bar{\boldsymbol{q}}_0 + \frac{T}{6}\left(\boldsymbol{d}_{n_1} + 2\boldsymbol{d}_{n_2} + 2\boldsymbol{d}_{n_3} + \boldsymbol{d}_{n_4}\right), \tag{10}$$

where

$$\boldsymbol{d}_{n_1} = \frac{1}{2}\boldsymbol{\Omega}\left[{}^{B}\hat{\boldsymbol{\omega}}_n(t_k)\right]\bar{\boldsymbol{q}}_0, \quad \boldsymbol{d}_{n_2} = \frac{1}{2}\boldsymbol{\Omega}\left[\bar{\boldsymbol{\omega}}_n\right]\cdot\left(\bar{\boldsymbol{q}}_0 + \frac{1}{2}T\boldsymbol{d}_{n_1}\right),$$

$$\boldsymbol{d}_{n_3} = \frac{1}{2}\boldsymbol{\Omega}\left[\bar{\boldsymbol{\omega}}_n\right]\cdot\left(\bar{\boldsymbol{q}}_0 + \frac{1}{2}T\boldsymbol{d}_{n_2}\right), \quad \boldsymbol{d}_{n_4} = \frac{1}{2}\boldsymbol{\Omega}\left[{}^{B}\hat{\boldsymbol{\omega}}_n(t_{k+1})\right]\cdot\left(\bar{\boldsymbol{q}}_0 + T\boldsymbol{d}_{n_3}\right),$$

$$\bar{\boldsymbol{q}}_0 \triangleq \left[0,\, 0,\, 0,\, 1\right]^{\mathsf{T}}, \quad \bar{\boldsymbol{\omega}}_n \triangleq \frac{1}{2}\left[{}^{B}\hat{\boldsymbol{\omega}}_n(t_{k+1}) + {}^{B}\hat{\boldsymbol{\omega}}_n(t_k)\right],$$

where ${}^{B}\hat{\boldsymbol{\omega}}_n(t_k) = \boldsymbol{\omega}_{\mathrm{imu}_n}(t_k) - \hat{\boldsymbol{b}}_{g_n}(k|j)$. There is no guarantee that the quaternion vector obtained in (10) will be a unit vector, and therefore it must be normalized, i.e., ${}^{B_{k+1}}_{B_k}\hat{\bar{\boldsymbol{q}}}_n \leftarrow {}^{B_{k+1}}_{B_k}\hat{\bar{\boldsymbol{q}}}_n \Big/ \left\|{}^{B_{k+1}}_{B_k}\hat{\bar{\boldsymbol{q}}}_n\right\|_2$. The orientation state estimate propagation equation becomes

$${}^{B_{k+1|j}}_{G}\hat{\bar{\boldsymbol{q}}}_n = {}^{B_{k+1}}_{B_k}\hat{\bar{\boldsymbol{q}}}_n \otimes {}^{B_{k|j}}_{G}\hat{\bar{\boldsymbol{q}}}_n.$$

The integral in (5) is solved using trapezoidal integration and the velocity state estimate is propagated according to

$$\hat{\boldsymbol{v}}_{r_n}(k+1|j) = \hat{\boldsymbol{v}}_{r_n}(k|j) + \frac{T}{2}\left[\hat{\boldsymbol{s}}_n(k) + \hat{\boldsymbol{s}}_n(k+1)\right] + {}^{G}\boldsymbol{g}_n(k)T,$$

where $\hat{\boldsymbol{s}}_n(k) \triangleq \hat{\mathbf{R}}_n^{\mathsf{T}}(k)\left[\boldsymbol{a}_{\mathrm{imu}_n}(t_k) - \hat{\boldsymbol{b}}_{a_n}(k|j)\right]$ and $\hat{\mathbf{R}}_n(k) \triangleq \mathbf{R}\left[{}^{B_{k|j}}_{G}\hat{\bar{\boldsymbol{q}}}_n\right]$. Similarly, the integral in (6) is solved using trapezoidal integration and the position state estimate is propagated according to

$$\hat{\boldsymbol{r}}_{r_n}(k+1|j) = \hat{\boldsymbol{r}}_{r_n}(k|j) + \frac{T}{2}\left[\hat{\boldsymbol{v}}_{r_n}(k+1|j) + \hat{\boldsymbol{v}}_{r_n}(k|j)\right].$$

Finally, the receiver's clock state estimate propagation follows from (2) and is given by

$$\hat{\boldsymbol{x}}_{\mathrm{clk},r_n}(k+1|j) = \mathbf{F}_{\mathrm{clk}}\hat{\boldsymbol{x}}_{\mathrm{clk},r_n}(k|j).$$

B.3 Covariance Propagation

During the collaborative mapping mode, the one-step prediction error covariance is given by

$$\mathbf{P}_{\boldsymbol{x}}(k+1|j) = \mathbf{F}\mathbf{P}_{\boldsymbol{x}}(k|j)\mathbf{F}^{\mathsf{T}} + \mathbf{Q}, \tag{11}$$

$$\mathbf{F} \triangleq \operatorname{diag}\left[\boldsymbol{\Phi}_{B_1}, \mathbf{F}_{\text{clk}}, \ldots, \boldsymbol{\Phi}_{B_N}, \mathbf{F}_{\text{clk}}, \mathbf{F}_{\text{sop}}, \ldots, \mathbf{F}_{\text{sop}}\right], \quad \mathbf{Q} \triangleq \operatorname{diag}\left[\mathbf{Q}_{r_1}, \ldots, \mathbf{Q}_{r_N}, \mathbf{Q}_{\text{sop}_1}, \ldots, \mathbf{Q}_{\text{sop}_M}\right],$$

where $\boldsymbol{\Phi}_{B_n}$ is the n^{th} AV's DT linearized INS state transition matrix and $\mathbf{Q}_{r_n} \triangleq \operatorname{diag}\left[\mathbf{Q}_{d,B_n}, c^2\mathbf{Q}_{\text{clk},r_n}\right]$, where $\mathbf{Q}_{d,B_n}$ is the n^{th} AV's DT linearized INS state process noise covariance. The DT linearized INS state transition matrix $\boldsymbol{\Phi}_{B_n}$ is given by

$$\boldsymbol{\Phi}_{B_n} = \begin{bmatrix} \mathbf{I}_{3\times3} & \mathbf{0}_{3\times3} & \mathbf{0}_{3\times3} & \boldsymbol{\Phi}_{\boldsymbol{qb}_{g_n}} & \boldsymbol{\Phi}_{\boldsymbol{qb}_{a_n}} \\ \boldsymbol{\Phi}_{\boldsymbol{pq}_n} & \mathbf{I}_{3\times3} & \mathbf{I}_{3\times3}T & \boldsymbol{\Phi}_{\boldsymbol{pb}_{g_n}} & \boldsymbol{\Phi}_{\boldsymbol{pb}_{a_n}} \\ \boldsymbol{\Phi}_{\boldsymbol{vq}_n} & \mathbf{0}_{3\times3} & \mathbf{I}_{3\times3} & \boldsymbol{\Phi}_{\boldsymbol{vb}_{g_n}} & \boldsymbol{\Phi}_{\boldsymbol{vb}_{a_n}} \\ \mathbf{0}_{3\times3} & \mathbf{0}_{3\times3} & \mathbf{0}_{3\times3} & \mathbf{I}_{3\times3} & \mathbf{0}_{3\times3} \\ \mathbf{0}_{3\times3} & \mathbf{0}_{3\times3} & \mathbf{0}_{3\times3} & \mathbf{0}_{3\times3} & \mathbf{I}_{3\times3} \end{bmatrix},$$

where

$$\boldsymbol{\Phi}_{\boldsymbol{vq}_n} = -\frac{T}{2}\left\lfloor[\hat{\boldsymbol{s}}_n(k) + \hat{\boldsymbol{s}}_n(k+1)]\times\right\rfloor, \quad \boldsymbol{\Phi}_{\boldsymbol{pq}_n} = \frac{T}{2}\boldsymbol{\Phi}_{\boldsymbol{vq}_n}, \quad \boldsymbol{\Phi}_{\boldsymbol{qb}_{g_n}} = -\frac{T}{2}\left[\hat{\mathbf{R}}_n^{\mathsf{T}}(k+1) + \hat{\mathbf{R}}_n^{\mathsf{T}}(k)\right], \quad \boldsymbol{\Phi}_{\boldsymbol{qb}_{a_n}} = -\boldsymbol{\Phi}_{\boldsymbol{qb}_{g_n}},$$

$$\boldsymbol{\Phi}_{\boldsymbol{vb}_{g_n}} = -\frac{T}{2}\left\lfloor\hat{\boldsymbol{s}}_n(k)\times\right\rfloor\boldsymbol{\Phi}_{\boldsymbol{qb}_{g_n}}, \quad \boldsymbol{\Phi}_{\boldsymbol{vb}_{a_n}} = \boldsymbol{\Phi}_{\boldsymbol{qb}_{g_n}} + \boldsymbol{\Phi}_{\boldsymbol{vb}_{g_n}}, \quad \boldsymbol{\Phi}_{\boldsymbol{pb}_{g_n}} = \frac{T}{2}\boldsymbol{\Phi}_{\boldsymbol{vb}_{g_n}}, \quad \boldsymbol{\Phi}_{\boldsymbol{pb}_{a_n}} = \frac{T}{2}\boldsymbol{\Phi}_{\boldsymbol{vb}_{a_n}}.$$

The DT linearized INS state process noise covariance $\mathbf{Q}_{d,B_n}$ is given by

$$\mathbf{Q}_{d,B_n} = \frac{T}{2}\boldsymbol{\Phi}_{B_n}^{\mathsf{T}}\mathbf{N}_{c_n}\boldsymbol{\Phi}_{B_n} + \mathbf{N}_{c_n},$$

where

$$\mathbf{N}_{c_n} = \operatorname{diag}\left[\sigma_{g_n}^2\mathbf{I}_{3\times3}, \mathbf{0}_{3\times3}, \sigma_{a_n}^2\mathbf{I}_{3\times3}, \sigma_{w_{g_n}}^2\mathbf{I}_{3\times3}, \sigma_{w_{a_n}}^2\mathbf{I}_{3\times3}\right].$$

The detailed derivations of $\boldsymbol{\Phi}_{B_n}$ and $\mathbf{Q}_{d,B_n}$ are described in [29, 34].

B.4 Measurement Update

When an INS-aiding source is available, the EKF update step will correct the INS and clock errors using the standard EKF update equations [35]. In the collaborative mapping mode, i.e., $\boldsymbol{z} \triangleq \left[\boldsymbol{z}_{\text{sv}}^{\mathsf{T}}, \boldsymbol{z}_{\text{sop}}^{\mathsf{T}}\right]^{\mathsf{T}}$, the corresponding Jacobian is

$$\mathbf{H} = \begin{bmatrix} \mathbf{H}_{\text{sv},r} & \mathbf{0}_{NL\times5M} \\ \mathbf{H}_{\text{sop},r} & \mathbf{H}_{\text{sop,sop}} \end{bmatrix}, \quad \mathbf{H}_{\text{sv},r} \triangleq \operatorname{diag}\left[\mathbf{H}_{\text{sv},r_1}, \ldots, \mathbf{H}_{\text{sv},r_N}\right], \quad \mathbf{H}_{\text{sop},r} \triangleq \operatorname{diag}\left[\mathbf{H}_{\text{sop},r_1}, \ldots, \mathbf{H}_{\text{sop},r_N}\right],$$

$$\mathbf{H}_{\text{sv},r_n} \triangleq \begin{bmatrix} \mathbf{0}_{1\times3} & \hat{\mathbf{1}}_{r_n,\text{sv}_1}^{\mathsf{T}} & \mathbf{0}_{1\times9} & \boldsymbol{h}_{\text{clk}}^{\mathsf{T}} \\ \vdots & \vdots & \vdots & \vdots \\ \mathbf{0}_{1\times3} & \hat{\mathbf{1}}_{r_n,\text{sv}_L}^{\mathsf{T}} & \mathbf{0}_{1\times9} & \boldsymbol{h}_{\text{clk}}^{\mathsf{T}} \end{bmatrix}, \quad \mathbf{H}_{\text{sop},r_n} \triangleq \begin{bmatrix} \mathbf{0}_{1\times3} & \hat{\mathbf{1}}_{r_n,\text{sop}_1}^{\mathsf{T}} & \mathbf{0}_{1\times9} & \boldsymbol{h}_{\text{clk}}^{\mathsf{T}} \\ \vdots & \vdots & \vdots & \vdots \\ \mathbf{0}_{1\times3} & \hat{\mathbf{1}}_{r_n,\text{sop}_M}^{\mathsf{T}} & \mathbf{0}_{1\times9} & \boldsymbol{h}_{\text{clk}}^{\mathsf{T}} \end{bmatrix},$$

$$\mathbf{H}_{\text{sop,sop}} \triangleq \left[\boldsymbol{\Psi}_{\text{sop},r_1}^{\mathsf{T}}, \ldots, \boldsymbol{\Psi}_{\text{sop},r_N}^{\mathsf{T}}\right]^{\mathsf{T}}, \quad \boldsymbol{\Psi}_{\text{sop},r_n} \triangleq \operatorname{diag}\left[\boldsymbol{\Psi}_{\text{sop}_1,r_n}, \ldots, \boldsymbol{\Psi}_{\text{sop}_M,r_n}\right],$$

where $\hat{\mathbf{1}}_{r_n,\text{sv}_l} \triangleq \frac{\hat{\boldsymbol{r}}_{r_n} - \boldsymbol{r}_{\text{sv}_l}}{\|\hat{\boldsymbol{r}}_{r_n} - \boldsymbol{r}_{\text{sv}_l}\|}$, $\boldsymbol{h}_{\text{clk}} \triangleq [1, 0]^{\mathsf{T}}$, $\hat{\mathbf{1}}_{r_n,\text{sop}_m} \triangleq \frac{\hat{\boldsymbol{r}}_{r_n} - \hat{\boldsymbol{r}}_{\text{sop}_m}}{\|\hat{\boldsymbol{r}}_{r_n} - \hat{\boldsymbol{r}}_{\text{sop}_m}\|}$, and $\boldsymbol{\Psi}_{\text{sop}_m,r_n} \triangleq \left[-\hat{\mathbf{1}}_{r_n,\text{sop}_m}^{\mathsf{T}}, -\boldsymbol{h}_{\text{clk}}^{\mathsf{T}}\right]$. Assuming uncorrelated pseudorange measurement noise, the measurement noise covariance is given by

$$\mathbf{R} = \operatorname{diag}\left[\mathbf{R}_{\text{sv}}, \mathbf{R}_{\text{sop}}\right], \quad \mathbf{R}_{\text{sv}} \triangleq \operatorname{diag}\left[\mathbf{R}_{r_1,\text{sv}}, \ldots, \mathbf{R}_{r_N,\text{sv}}\right], \quad \mathbf{R}_{\text{sop}} \triangleq \operatorname{diag}\left[\mathbf{R}_{r_1,\text{sop}}, \ldots, \mathbf{R}_{r_N,\text{sop}}\right],$$

where $\mathbf{R}_{r_n,\text{sv}} \triangleq \operatorname{diag}\left[\sigma_{r_n,\text{sv}_1}^2, \ldots, \sigma_{r_n,\text{sv}_L}^2\right]$ and $\mathbf{R}_{r_n,\text{sop}} \triangleq \operatorname{diag}\left[\sigma_{r_n,\text{sop}_1}^2, \ldots, \sigma_{r_n,\text{sop}_M}^2\right]$. The update will produce the posterior estimate $\hat{\boldsymbol{x}}(j|j)$ and an associated posterior estimation error covariance $\mathbf{P}_{\boldsymbol{x}}(j|j)$.

C. C-SLAM Mode

In the C-SLAM mode, TDOA measurements taken in reference to the first SOP are used, i.e., the measurement from the n^{th} AV-mounted receiver to the m^{th} SOP becomes $z'_{r_n,\text{sop}_m} \triangleq z_{r_n,\text{sop}_m} - z_{r_n,\text{sop}_1}$. The time bias in such measurement is parameterized only by the clock biases of the SOPs, hence the receivers' clock biases no longer need to be estimated. Moreover, the difference of the SOPs' clock biases is estimated instead of the individual clock biases. The EKF implementation of this mode is discussed next.

C.1 Error State Model

In the C-SLAM mode the EKF produces an estimate $\hat{\boldsymbol{x}}'(k|j) \triangleq \mathbb{E}[\boldsymbol{x}'(k)|\{\boldsymbol{z}'(i)\}_{i=1}^{j}]$ of $\boldsymbol{x}(k)$, and an associated estimation error covariance $\mathbf{P}_{\boldsymbol{x}'}(k|j) \triangleq \mathbb{E}[\tilde{\boldsymbol{x}}'(k|j)\tilde{\boldsymbol{x}}'^{\mathsf{T}}(k|j)]$ where

$$\boldsymbol{x}' \triangleq \left[\boldsymbol{x}_{B_1}^{\mathsf{T}}, \ldots, \boldsymbol{x}_{B_N}^{\mathsf{T}}, \boldsymbol{r}_{\text{sop}_1}^{\mathsf{T}}, \boldsymbol{r}_{\text{sop}_2}^{\mathsf{T}}, \boldsymbol{\Delta x}_{\text{clk,sop}_2}^{\mathsf{T}}, \ldots, \boldsymbol{r}_{\text{sop}_M}^{\mathsf{T}}, \boldsymbol{\Delta x}_{\text{clk,sop}_M}^{\mathsf{T}}\right]^{\mathsf{T}}, \quad \boldsymbol{\Delta x}_{\text{clk,sop}_m} \triangleq \left[c\Delta\delta t_{\text{clk,sop}_m}, c\Delta\dot{\delta} t_{\text{clk,sop}_m}\right]^{\mathsf{T}},$$

where $c\Delta\delta t_{\text{clk,sop}_m} \triangleq c\delta t_{\text{sop}_m} - c\delta t_{\text{sop}_1}$ and $c\Delta\dot{\delta} t_{\text{clk,sop}_m} \triangleq c\dot{\delta} t_{\text{sop}_m} - c\dot{\delta} t_{\text{sop}_1}$, and the new set of measurements $\boldsymbol{z}'$ are

$$\boldsymbol{z}' = \mathbf{T}_{\boldsymbol{z}}\boldsymbol{z}_{\text{sop}} = \left[\boldsymbol{z}'^{\mathsf{T}}_{r_1,\text{sop}}, \ldots, \boldsymbol{z}'^{\mathsf{T}}_{r_N,\text{sop}}\right]^{\mathsf{T}}, \quad \boldsymbol{z}'^{\mathsf{T}}_{r_n,\text{sop}} \triangleq \left[z'_{r_n,\text{sop}_2}, \ldots, z'_{r_n,\text{sop}_M}\right]^{\mathsf{T}},$$

where $\mathbf{T}_{\boldsymbol{z}}$ is the transformation that maps $\boldsymbol{z}$ to $\boldsymbol{z}'$. The EKF error state is defined as

$$\tilde{\boldsymbol{x}}' \triangleq \left[\tilde{\boldsymbol{x}}_{B_1}^{\mathsf{T}}, \ldots, \tilde{\boldsymbol{x}}_{B_N}^{\mathsf{T}}, \tilde{\boldsymbol{r}}_{\text{sop}_1}^{\mathsf{T}}, \tilde{\boldsymbol{r}}_{\text{sop}_2}^{\mathsf{T}}, \boldsymbol{\Delta}\tilde{\boldsymbol{x}}_{\text{clk,sop}_2}^{\mathsf{T}}, \ldots, \tilde{\boldsymbol{r}}_{\text{sop}_M}^{\mathsf{T}}, \boldsymbol{\Delta}\tilde{\boldsymbol{x}}_{\text{clk,sop}_M}^{\mathsf{T}}\right]^{\mathsf{T}}. \tag{12}$$

C.2 State and Covariance Propagation

In this mode, the AVs' INS states and SOPs' position states are propagated using the same equations as in the collaborative mapping mode. The new clock states are propagated according to $\boldsymbol{\Delta}\hat{\boldsymbol{x}}_{\text{clk,sop}_m}(k+1|j) = \mathbf{F}_{\text{clk}}\,\boldsymbol{\Delta}\hat{\boldsymbol{x}}_{\text{clk,sop}_m}(k|j)$.

The prediction error covariance $\mathbf{P}_{\boldsymbol{x}'}(k+1|j)$ has the same form as (11), except that $\mathbf{F}$ and $\mathbf{Q}$ are replaced with $\mathbf{F}'$ and $\mathbf{Q}'$, respectively, where

$$\mathbf{F}' \triangleq \text{diag}[\boldsymbol{\Phi}_{B_1}, \ldots, \boldsymbol{\Phi}_{B_N}, \mathbf{I}_{3\times 3}, \mathbf{F}_{\text{sop}}, \ldots, \mathbf{F}_{\text{sop}}], \quad \mathbf{Q}' = \mathbf{T}_{\boldsymbol{x}}\mathbf{Q}\mathbf{T}_{\boldsymbol{x}}^{\mathsf{T}},$$

where $\mathbf{T}_{\boldsymbol{x}}$ is the transformation that maps $\tilde{\boldsymbol{x}}$ to $\tilde{\boldsymbol{x}}'$.

C.3 Measurement Update

The C-SLAM mode update step is similar to the collaborative mapping mode update except the measurement Jacobian is replaced with

$$\mathbf{H}' = \left[\mathbf{H}'_B, \mathbf{H}'_{\text{sop}}\right], \quad \mathbf{H}'_B \triangleq \text{diag}\left[\mathbf{H}'_{B_1}, \ldots, \mathbf{H}'_{B_N}\right], \quad \mathbf{H}'_{\text{sop}} \triangleq \left[\mathbf{H}'^{\mathsf{T}}_{\text{sop},r_1}, \ldots, \mathbf{H}'^{\mathsf{T}}_{\text{sop},r_N}\right]^{\mathsf{T}},$$

$$\mathbf{H}'_{B_n} \triangleq \begin{bmatrix} \mathbf{0}_{1\times 3} & \hat{\mathbf{l}}_{r_n,\text{sop}_2} - \hat{\mathbf{l}}_{r_n,\text{sop}_1} & \mathbf{0}_{1\times 9} \\ \vdots & \vdots & \vdots \\ \mathbf{0}_{1\times 3} & \hat{\mathbf{l}}_{r_n,\text{sop}_M} - \hat{\mathbf{l}}_{r_n,\text{sop}_1} & \mathbf{0}_{1\times 9} \end{bmatrix}, \quad \mathbf{H}'_{\text{sop},r_n} \triangleq \begin{bmatrix} \hat{\mathbf{l}}_{r_n,\text{sop}_1} & \boldsymbol{\Psi}_{\text{sop}_2,r_n} & \cdots & \mathbf{0} \\ \vdots & \vdots & \ddots & \vdots \\ \hat{\mathbf{l}}_{r_n,\text{sop}_1} & \mathbf{0} & \cdots & \boldsymbol{\Psi}_{\text{sop}_M,r_n} \end{bmatrix},$$

and the measurement noise covariance is replaced with $\mathbf{R}' = \mathbf{T}_{\boldsymbol{z}}\mathbf{R}_{\text{sop}}\mathbf{T}_{\boldsymbol{z}}^{\mathsf{T}}$. The update will produce the posterior estimate $\hat{\boldsymbol{x}}'(j|j)$ and an associated posterior estimation error covariance $\mathbf{P}_{\boldsymbol{x}'}(j|j)$.

IV. Simulation results

In this section, the estimation performance of the collaborative SOP-aided INS framework described in Section III is analyzed using a simulator which generated (i) the true states of the navigating AVs, (ii) the SOPs' states, (iii) noise-corrupted IMU measurements of specific force $\boldsymbol{a}_{\text{imu}_n}$ and angular rates $\boldsymbol{\omega}_{\text{imu}_n}$ for each vehicle, and (iv) noise-corrupted pseudoranges from each vehicle to multiple SOPs and GPS SVs. Details of this simulator are provided next.

A. Simulator

The states of N AVs were simulated. Each AV-mounted receiver was set to be equipped with a typical temperature-compensated crystal oscillator (TCXO), with $\{h_{0,r_n}, h_{-2,r_n}\} = \{9.4 \times 10^{-20}, 3.8 \times 10^{-21}\}$, where $n = 1, ..., N$. Each simulated trajectory corresponded to an unmanned aerial vehicle (UAV), which included two straight segments, a climb, and a repeating orbit, performed over a 200 second period. The trajectories were generated using a standard six degree-of-freedom (6DoF) kinematic model for airplanes [29]. Excluding trajectories generated in a closed-loop fashion so to optimize the vehicles' and SOPs' estimates [36], this type of open-loop trajectory has been demonstrated to produce better estimates than an open-loop random trajectory [37, 38].

The IMU signal generator models a triad gyroscope and a triad accelerometer. The data $y_i(t)$ for the i^{th} axis of the gyroscope and accelerometer were generated at $T = 100$ Hz according to

$$y_i(t) = (1 + \epsilon_{k_i}) \cdot [u_i(t) + b_i(t) + \eta_{MA_i} + \eta_{Q_i} + \eta_{RRW_i} + \eta_{RR_i}],$$

where $u_i(t)$ is either the vehicle's actual acceleration or angular rotation rate for axis i, ϵ_{k_i} is the scale factor, $b_i(t)$ is a random bias which is driven by the bias instability, η_{MA_i} is the misalignment, η_{Q_i} is quantization noise, η_{RRW_i} is rate random walk, and η_{RR_i} is rate ramp [39]. The magnitude of these errors and their driving statistics are determined by the grade of the IMU. Data for a consumer-grade IMU was generated for this work.

GPS L1 C/A pseudoranges were generated at 1 Hz according to (8) using SV orbits produced from Receiver Independent Exchange (RINEX) files downloaded on October 22, 2016 from a Continuously Operating Reference Station (CORS) server [40]. They were set to be available for $t \in [0, 50)$ seconds, and unavailable for $t \in [50, 200]$ seconds. Pseudoranges were generated to six SOPs at 5 Hz according to (7) and the SOP dynamics discussed in Subsection II-A. Each SOP was set to be equipped with a typical oven-controlled crystal oscillator (OCXO), with $\{h_{0,\text{sop}_m}, h_{-2,\text{sop}_m}\} = \{8 \times 10^{-20}, 4 \times 10^{-23}\}$, where $m = 1, ..., 6$. The SOP emitter positions $\{\boldsymbol{r}_{\text{sop}_m}\}_{m=1}^{6}$ were surveyed from cellular tower locations in downtown Los Angeles, California. The simulated trajectories, SOP positions, and the vehicles' positions at the time GPS was set to become unavailable are illustrated in Fig. 2.

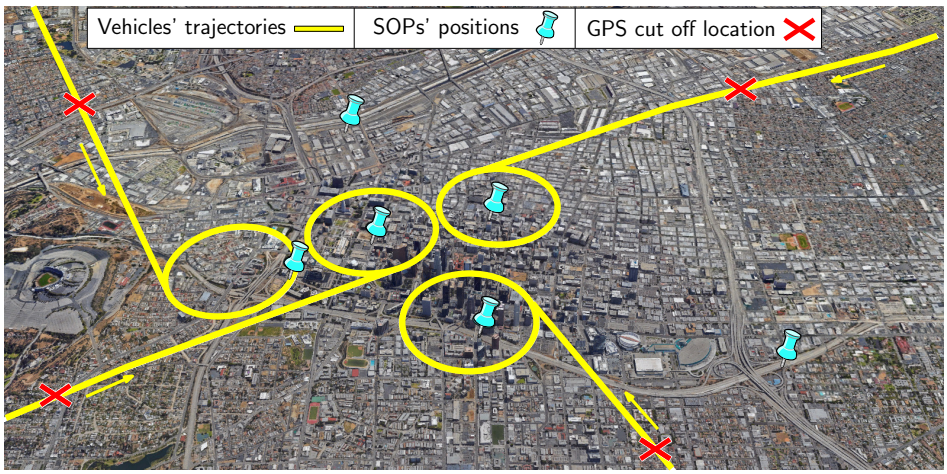

Fig. 2. True UAVs' traversed trajectories (yellow), SOP locations (blue pins), and the vehicles' positions at the time GPS was cut off (red).

B. Results

To demonstrate the performance of the collaborative SOP aided-INS framework, the environment described in Subsection IV-A was simulated. Two scenarios were considered: (i) an environment consisting of four AVs ($N = 4$) and (ii) an environment consisting of a single AV ($N = 1$). Each vehicle was assumed to be equipped with a consumer-grade IMU and have access to pseudoranges drawn from the same six SOPs ($M = 6$). The initial errors of the navigating AVs' states were initialized according to $\tilde{\boldsymbol{x}}_{r_n}(0|0) \sim \mathcal{N}\left[\mathbf{0}_{17\times 1}, \mathbf{P}_{\boldsymbol{x}_{r_n}}(0|0)\right]$, where $\mathbf{P}_{\boldsymbol{x}_{r_n}}(0|0) \equiv \text{diag}\left[(10^{-2}) \cdot \mathbf{I}_{3\times 3}, 9 \cdot \mathbf{I}_{3\times 3}, \mathbf{I}_{3\times 3}, (10^{-6}) \cdot \mathbf{I}_{6\times 6}, 9, 1\right]$ for $n = 1, \ldots, 4$. The SOP state estimates were initialized

according to $\hat{\boldsymbol{x}}_{\mathrm{sop}_m}(0|0) \sim \mathcal{N}\left[\boldsymbol{x}_{\mathrm{sop}_m}(0), \mathbf{P}_{\mathrm{sop}}(0|0)\right]$, for $m = 1, \ldots, 6$, where $\boldsymbol{x}_{\mathrm{sop}_m}(0) \equiv \left[\boldsymbol{r}^{\mathsf{T}}_{\mathrm{sop}_m},\, 10^4, 10\right]^{\mathsf{T}}$, $\mathbf{P}_{\mathrm{sop}}(0|0) \equiv (10^4) \cdot \mathrm{diag}\,[1,\, 1,\, 1,\, 0.1,\, 0.01]$.

The resulting estimation error trajectories and corresponding 3σ bounds for the position, velocity, and attitude of one of the AVs and the position of one of the SOPs are plotted in Figs. 3 (a)-(l). For a comparative analysis, the 3σ bounds produced by a traditional GPS-aided INS are also plotted. The plots in Figs. 4 (a) and (b) correspond to the estimation errors of the receiver's clock states with GPS available and the plots in Figs. 4 (c) and (d) correspond to the estimation errors of the SOP's clock states while GPS was available. Figs. 4 (e) and (f) correspond to the estimation errors of the relative SOP clock biases and drifts that were initialized when GPS became unavailable, as was described in Subsection III-C.1.

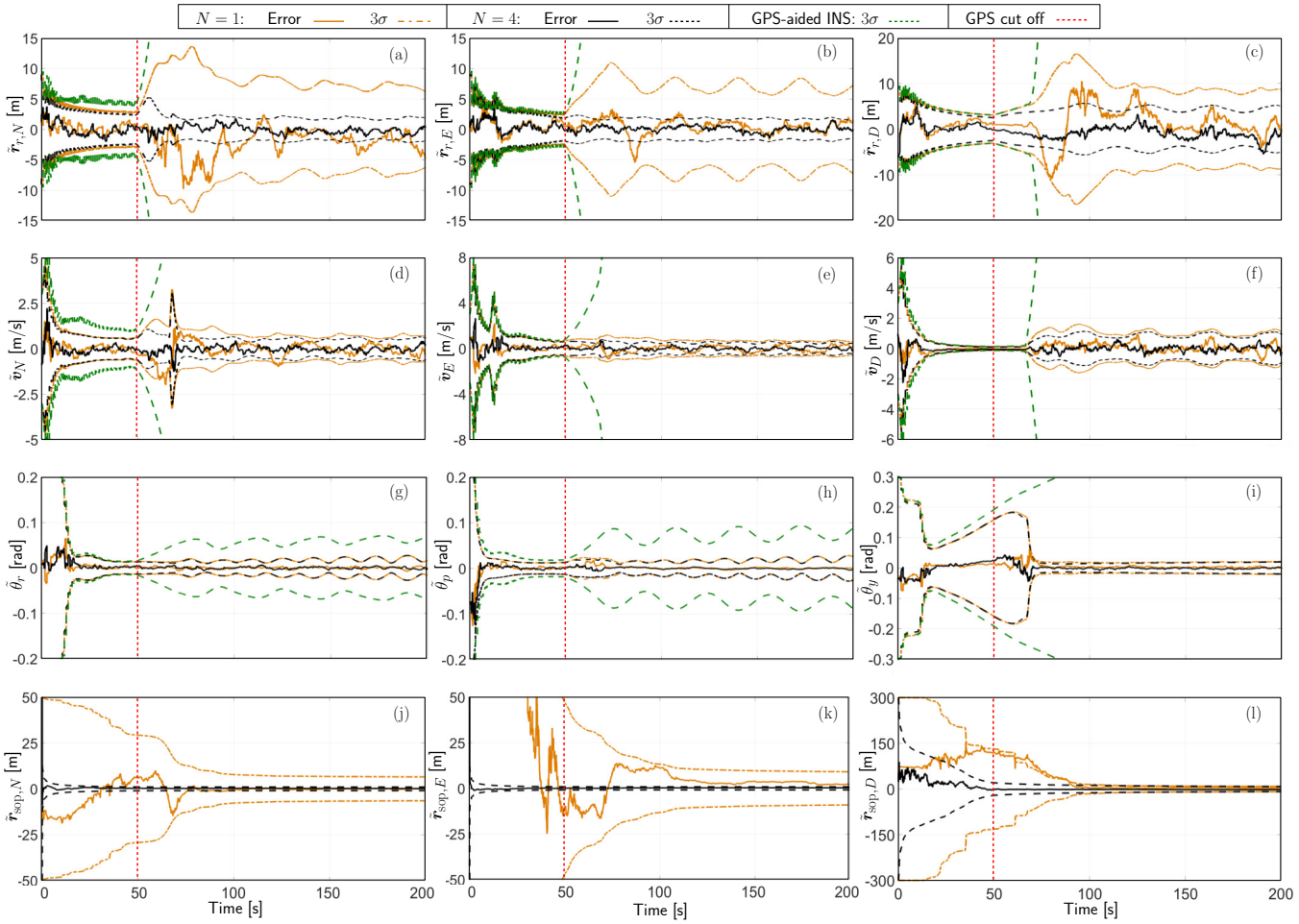

Fig. 3. The results of two scenarios are illustrated. In both scenarios, each navigating UAV had access to GPS pseudoranges for only the first 50 seconds while traversing the trajectories illustrated in Fig. 2. In the first scenario, four AVs ($N = 4$) using a centralized collaborative SOP-aided INS produced the estimation error trajectories and corresponding 3σ bounds (black). In the second scenario, one AV ($N = 1$) with an SOP-aided INS produced the estimation error trajectories and corresponding 3σ bounds (orange). For a comparative analysis, the 3σ bounds for a traditional GPS-aided INS are shown (green). North, East, and down (NED) errors are shown for position and velocity. Roll, pitch, and yaw (rpy) errors are shown for the orientation.

The following may be concluded from these plots. First, without aiding, the estimation error uncertainties diverge (as expected), but with SOP aiding, the error uncertainties are bounded (in the absence of GPS). Second, the produced estimation uncertainties of the position states for both the AV and the SOP when $N = 4$ are significantly less than the ones produced when $N = 1$. Moreover, the estimator's transient phase for both the AV and the SOP when $N = 4$ is shorter than the transient phase when $N = 1$, especially for the SOP's position states.

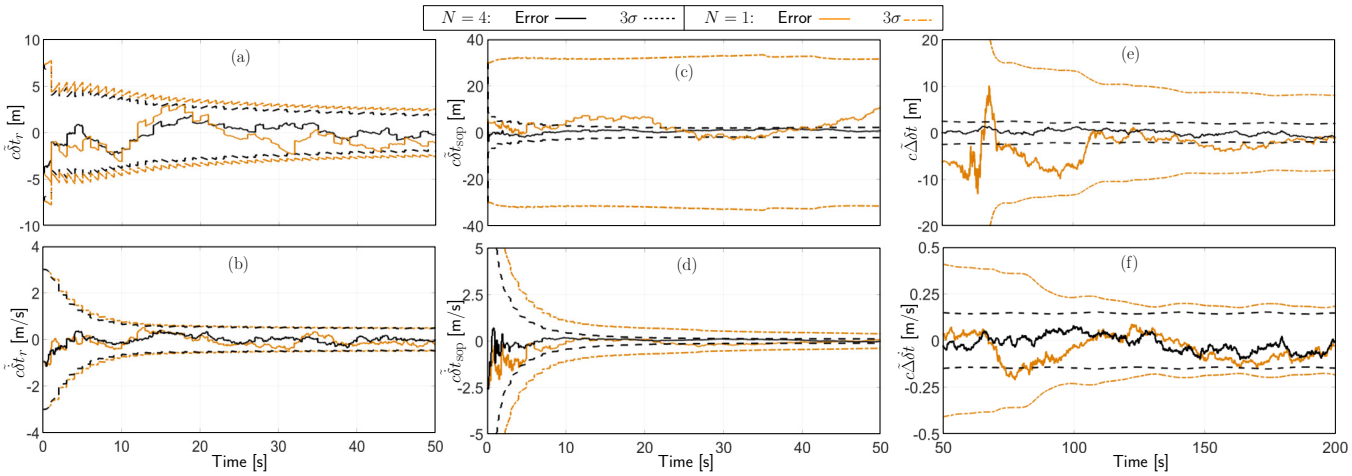

Fig. 4. Estimation error trajectories and 3σ bounds for four AVs ($N = 4$) using a centralized collaborative SOP-aided INS (black) and a single AV ($N = 1$) using an SOP-aided INS (orange). (a) and (b) correspond to the receiver's clock states while GPS was available and (c) and (d) correspond to the SOP's clock states while GPS was available. (e) and (f) correspond to $\boldsymbol{\Delta x}_{\text{clk,sop}_2}$ during the C-SLAM mode.

B.1 Performance Analysis: Quantity of Collaborating AVs

To study the performance of the collaborative SOP-aided INS framework over a varying number of collaborating AVs, six separate simulation runs were conducted: four runs where the collaborative SOP-aided INS framework was employed ($N = 1, ..., 4$) and two runs where a traditional GPS-aided INS is used ($N = 1$). One of the GPS-aided INS runs uses only an INS after the GPS cut off time, while the other assumes GPS to be available during the entire run. Fig. 5 illustrates the resulting $\log\{\det[\mathbf{P}_{\boldsymbol{r}_r}]\}$ for each run, which is related to the volume of the uncertainty ellipsoid [38].

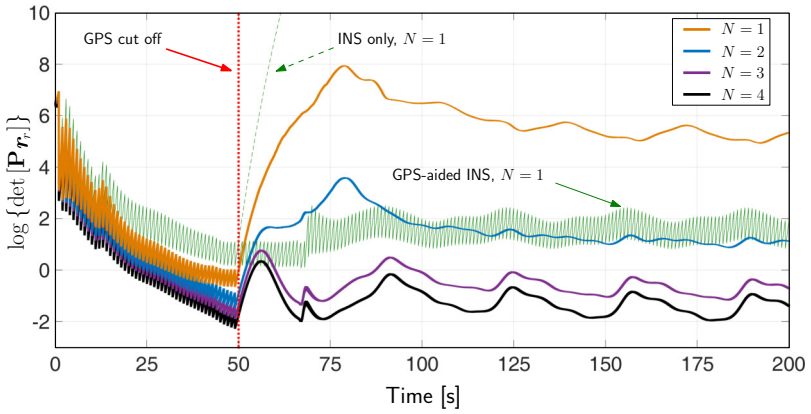

Fig. 5. Multiple UAVs traverse the trajectories illustrated in Fig. 2. GPS pseudoranges become unavailable at 50s (red dotted line) and the N vehicles continue to navigate using C-SLAM as described in Subsection III-C. The logarithm of the determinant of the estimation error covariance for the position of one of the AVs is plotted for a varying number of total collaborators N. Moreover, the logarithm of the determinant of the estimation error covariance for the position of one of the AVs navigating using (i) a traditional GPS-aided INS with continuous GPS access (green) and (ii) an INS only (green dashed) is plotted for comparison.

The following may be concluded from Fig. 5 about the collaborative SOP-aided INS framework. First, a bound may be specified on the estimation uncertainties for any number of collaborating AVs in the environment. Second, the estimation performance is always improved as more collaborating AVs are added to the environment. However, this performance improvement, which is captured by the distance between the $\log\{\det[\mathbf{P}_{\boldsymbol{r}_r}]\}$ curves, becomes less significant as the number of collaborating AVs increases. The maximum improvement is obtained when going from one AV to two collaborating AVs. Third, when GPS becomes unavailable, the collaborative SOP-aided INS will perform significantly better than an INS only for any number of collaborating AVs in the environment. Fourth, two or more collaborating AVs equipped with SOP-aided INSs which are in the absence of GPS signals can achieve

estimation performance comparable to one AV equipped with a traditional GPS-aided INS with access to GPS signals from eleven GPS SVs.

V. EXPERIMENTAL RESULTS

A field experiment was conducted using two IMU-equipped UAVs and software-defined receivers (SDRs) to demonstrate the collaborative SOP-aided INS framework discussed in Section III. To this end, two antennas were mounted on each UAV to acquire and track GPS signals and multiple cellular base transceiver stations (BTSs) whose signals were modulated through code division multiple access (CDMA). The GPS and cellular signals were simultaneously downmixed and synchronously sampled via two-channel Ettus® universal software radio peripherals (USRPs). These front-ends fed their data to the Multichannel Adaptive TRansceiver Information eXtractor (MATRIX) SDR, which produced pseudorange observables from all GPS L1 C/A signals in view and two cellular BTSs [6]. The IMU data was sampled from the UAV's on-board proprietary navigation system, which was developed by Autel Robotics®. Fig. 6 depicts the experimental hardware setup and Fig. 7 (a) illustrates the experimental environment.

Experimental results are presented for two estimators: (i) the collaborative SOP-aided INS described in this paper and (ii) for comparative analysis, a traditional GPS-aided INS using the UAV's IMU. The UAVs traversed the white trajectories plotted in Figs. 7 (c) and (d), which consist of GPS unavailability runs of 15 seconds. The North-East root mean squared errors (RMSEs) of the GPS-aided INSs' navigation solutions after GPS became unavailable were 9.9 and 14.55 meters, respectively. The UAVs also collaboratively estimated their trajectories using C-SLAM using the two cellular BTSs illustrated in Figs. 7 (b) and (e) to aid their on-board INSs. The North-East RMSEs of the UAVs' trajectories were 4.03 and 4.34 meters, respectively, and the final localization error of the cellular BTSs were 25.9 and 11.5 meters, respectively. The North-East 99$^{\text{th}}$-percentile initial and final uncertainty ellipses of the BTSs position states are illustrated in Fig. 7 (a). The UAVs' RMSEs and final errors are tabulated in Table I. It is worth noting that only two cellular BTSs were exploited in this experiment. The RMSE reduction from the collaborative SOP-aided INS will be even more significant when more SOPs are included.

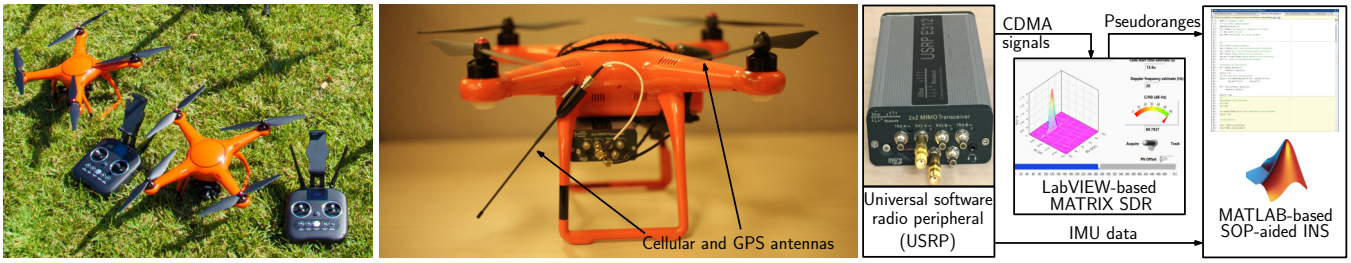

Fig. 6. Experiment hardware setup.

TABLE I
EXPERIMENTAL ESTIMATION ERRORS

Framework	Unaided INS		SOP-aided INS (C-SLAM)	
Vehicle	UAV 1	UAV 2	UAV 1	UAV 2
RMSE (m)	9.9	14.5	4.0	4.3
Final Error (m)	27.8	24.5	6.3	4.3

VI. CONCLUSION

This paper presented and studied a collaborative SOP-aided INS framework. Details of the framework were presented for implementation. Its performance was studied over a varying number of collaborating AVs and was shown to produce position estimation uncertainties comparable to a traditional GPS-aided INS when two or more AVs collaborated. Moreover, experimental results demonstrated two UAVs navigating with the collaborative SOP-aided INS framework using two cellular BTSs in the absence of GPS, which yielded UAV trajectory RMSE reductions of 59.3% and 70.2%, respectively, when compared to unaided INSs.

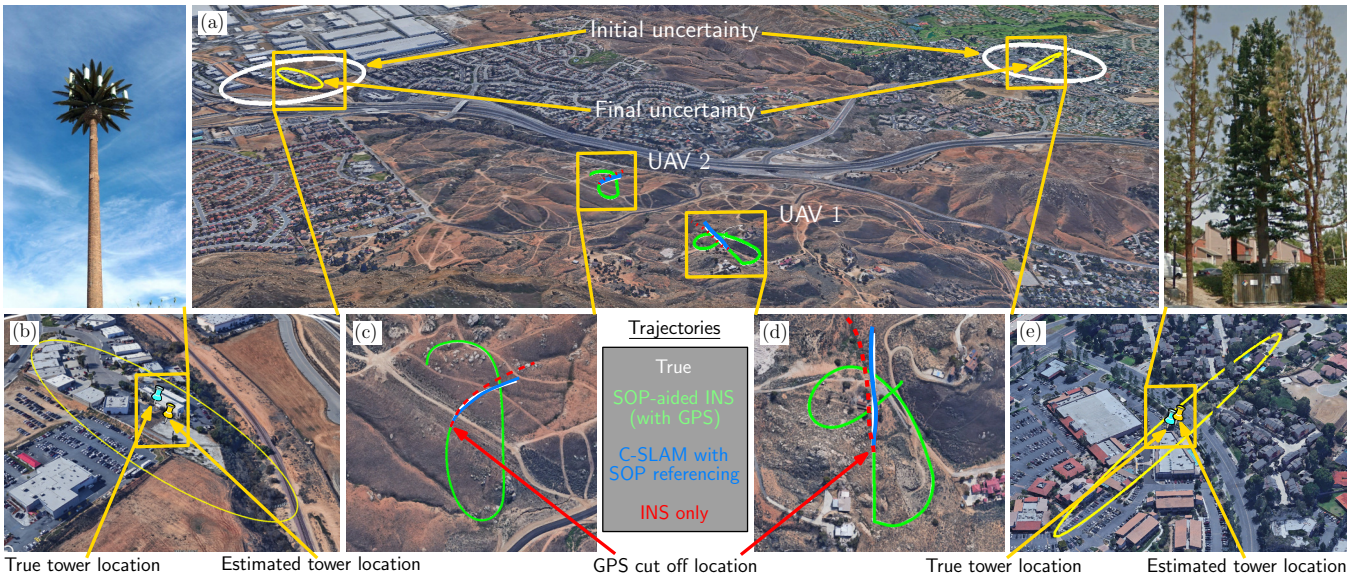

Fig. 7. Experimental results.

Acknowledgment

This work was supported in part by the Office of Naval Research (ONR) under Grant N00014-16-1-2305. The authors would like to thank Paul Roysdon for the simulated AV trajectories and Gogol Bhattacharya, Jesse Garcia, and Luting Yang for their help with data collection.

References

[1] J. Raquet and R. Martin, "Non-GNSS radio frequency navigation," in *Proceedings of IEEE International Conference on Acoustics, Speech and Signal Processing*, March 2008, pp. 5308–5311.
[2] L. Merry, R. Faragher, and S. Schedin, "Comparison of opportunistic signals for localisation," in *Proceedings of IFAC Symposium on Intelligent Autonomous Vehicles*, September 2010, pp. 109–114.
[3] K. Pesyna, Z. Kassas, J. Bhatti, and T. Humphreys, "Tightly-coupled opportunistic navigation for deep urban and indoor positioning," in *Proceedings of ION GNSS Conference*, September 2011, pp. 3605–3617.
[4] Z. Kassas, "Collaborative opportunistic navigation," *IEEE Aerospace and Electronic Systems Magazine*, vol. 28, no. 6, pp. 38–41, 2013.
[5] ——, "Analysis and synthesis of collaborative opportunistic navigation systems," Ph.D. dissertation, The University of Texas at Austin, USA, 2014.
[6] J. Khalife, K. Shamaei, and Z. Kassas, "A software-defined receiver architecture for cellular CDMA-based navigation," in *Proceedings of IEEE/ION Position, Location, and Navigation Symposium*, April 2016, pp. 816–826.
[7] K. Shamaei, J. Khalife, and Z. Kassas, "Performance characterization of positioning in LTE systems," in *Proceedings of ION GNSS Conference*, September 2016, pp. 2262–2270.
[8] ——, "Comparative results for positioning with secondary synchronization signal versus cell specific reference signal in LTE systems," in *Proceedings of ION International Technical Meeting Conference*, January 2017, accepted.
[9] J. Morales, P. Roysdon, and Z. Kassas, "Signals of opportunity aided inertial navigation," in *Proceedings of ION GNSS Conference*, September 2016, pp. 1492–1501.
[10] D. Gebre-Egziabher, "What is the difference between 'loose', 'tight', 'ultra-tight' and 'deep' integration strategies for INS and GNSS," *Inside GNSS*, pp. 28–33, January 2007.
[11] G. Panahandeh and M. Jansson, "Vision-aided inertial navigation based on ground plane feature detection," *IEEE/ASME Transactions on Mechatronics*, vol. 19, no. 4, pp. 1206–1215, August 2014.
[12] A. Soloviev, "Tight coupling of GPS and INS for urban navigation," *IEEE Transactions on Aerospace and Electronic Systems*, vol. 46, no. 4, pp. 1731–1746, October 2010.
[13] G. Grenon, P. An, S. Smith, and A. Healey, "Enhancement of the inertial navigation system for the morpheus autonomous underwater vehicles," *IEEE Journal of Oceanic Engineering*, vol. 26, no. 4, pp. 548–560, October 2001.
[14] J. McEllroy, "Navigation using signals of opportunity in the AM transmission band," Master's thesis, Air Force Institute of Technology, Wright-Patterson Air Force Base, Ohio, USA, 2006.
[15] S. Fang, J. Chen, H. Huang, and T. Lin, "Is FM a RF-based positioning solution in a metropolitan-scale environment? A probabilistic approach with radio measurements analysis," *IEEE Transactions on Broadcasting*, vol. 55, no. 3, pp. 577–588, September 2009.
[16] C. Yang, T. Nguyen, and E. Blasch, "Mobile positioning via fusion of mixed signals of opportunity," *IEEE Aerospace and Electronic Systems Magazine*, vol. 29, no. 4, pp. 34–46, April 2014.
[17] J. Morales, J. Khalife, and Z. Kassas, "Opportunity for accuracy," *GPS World Magazine*, vol. 27, no. 3, pp. 22–29, March 2016.
[18] M. Rabinowitz and J. Spilker, Jr., "A new positioning system using television synchronization signals," *IEEE Transactions on Broadcasting*, vol. 51, no. 1, pp. 51–61, March 2005.

[19] P. Thevenon, S. Damien, O. Julien, C. Macabiau, M. Bousquet, L. Ries, and S. Corazza, "Positioning using mobile TV based on the DVB-SH standard," *NAVIGATION, Journal of the Institute of Navigation*, vol. 58, no. 2, pp. 71–90, 2011.
[20] M. Joerger, L. Gratton, B. Pervan, and C. Cohen, "Analysis of Iridium-augmented GPS for floating carrier phase positioning," *NAVIGATION, Journal of the Institute of Navigation*, vol. 57, no. 2, pp. 137–160, 2010.
[21] K. Pesyna, Z. Kassas, and T. Humphreys, "Constructing a continuous phase time history from TDMA signals for opportunistic navigation," in *Proceedings of IEEE/ION Position Location and Navigation Symposium*, April 2012, pp. 1209–1220.
[22] I. Bisio, M. Cerruti, F. Lavagetto, M. Marchese, M. Pastorino, A. Randazzo, and A. Sciarrone, "A trainingless WiFi fingerprint positioning approach over mobile devices," *IEEE Antennas and Wireless Propagation Letters*, vol. 13, pp. 832–835, 2014.
[23] J. Khalife, Z. Kassas, and S. Saab, "Indoor localization based on floor plans and power maps: Non-line of sight to virtual line of sight," in *Proceedings of ION GNSS Conference*, September 2015, pp. 2291–2300.
[24] P. MacDoran, M. Mathews, K. Gold, and J. Alvarez, "Multi-sensors, signals of opportunity augmented GPS/GNSS challenged navigation," in *Proceedings of ION International Technical Meeting Conference*, September 2013, pp. 2552–2561.
[25] H. Durrant-Whyte and T. Bailey, "Simultaneous localization and mapping: part I," *IEEE Robotics & Automation Magazine*, vol. 13, no. 2, pp. 99–110, June 2006.
[26] A. Howard, "Multi-robot simultaneous localization and mapping using particle filters," *The International Journal of Robotics Research*, vol. 25, no. 12, pp. 1243–1256, December 2006.
[27] A. Thompson, J. Moran, and G. Swenson, *Interferometry and Synthesis in Radio Astronomy*, 2nd ed. John Wiley & Sons, 2001.
[28] N. Trawny and S. Roumeliotis, "Indirect Kalman filter for 3D attitude estimation," University of Minnesota, Dept. of Comp. Sci. & Eng., Tech. Rep. 2005-002, March 2005.
[29] P. Groves, *Principles of* GNSS*, Inertial, and Multisensor Integrated Navigation Systems*, 2nd ed. Artech House, 2013.
[30] M. Shelley, "Monocular visual inertial odometry," Master's thesis, Technical University of Munich, Germany, 2014.
[31] Z. Kassas and T. Humphreys, "Observability analysis of collaborative opportunistic navigation with pseudorange measurements," *IEEE Transactions on Intelligent Transportation Systems*, vol. 15, no. 1, pp. 260–273, February 2014.
[32] Z. Kassas, V. Ghadiok, and T. Humphreys, "Adaptive estimation of signals of opportunity," in *Proceedings of ION GNSS Conference*, September 2014, pp. 1679–1689.
[33] J. Morales and Z. Kassas, "Optimal receiver placement for collaborative mapping of signals of opportunity," in *Proceedings of ION GNSS Conference*, September 2015, pp. 2362–2368.
[34] J. Farrel and M. M. Barth, *The Global Positioning System and Inertial Navigation*. New York: McGraw-Hill, 1998.
[35] Y. Bar-Shalom, X. Li, and T. Kirubarajan, *Estimation with Applications to Tracking and Navigation*. New York, NY: John Wiley & Sons, 2002.
[36] Z. Kassas and T. Humphreys, "Receding horizon trajectory optimization in opportunistic navigation environments," *IEEE Transactions on Aerospace and Electronic Systems*, vol. 51, no. 2, pp. 866–877, April 2015.
[37] ——, "Motion planning for optimal information gathering in opportunistic navigation systems," in *Proceedings of AIAA Guidance, Navigation, and Control Conference*, August 2013, 551–4565.
[38] Z. Kassas, A. Arapostathis, and T. Humphreys, "Greedy motion planning for simultaneous signal landscape mapping and receiver localization," *IEEE Journal of Selected Topics in Signal Processing*, vol. 9, no. 2, pp. 247–258, March 2015.
[39] IEEE, "IEEE standard specification format guide and test procedure for linear, single-axis, non-gyroscopic accelerometers," IEEE, Tech. Rep. IEEE Std. 1293-1998 (R2008), July 2011.
[40] R. Snay and M. Soler, "Continuously operating reference station (CORS): history, applications, and future enhancements," *Journal of Surveying Engineering*, vol. 134, no. 4, pp. 95–104, November 2008.